Available online at www.sciencedirect.com
SCIENCE DIRECT®
International Journal of Heat and Mass Transfer 47 (2004) 3721–3743
International Journal of HEAT and MASS TRANSFER
www.elsevier.com/locate/ijhmt

Aiding and opposing contributions of centrifugal buoyancy on turbulent heat transfer in a two-pass transverse- or angled-rib-roughened channel with sharp 180° turns

Akira Murata [a,*], Sadanari Mochizuki [b]

[a] Department of Mechanical Systems Engineering, College of Engineering, Tokyo University of Agriculture and Technology, 2-24-16 Nakacho, Koganei, Tokyo 184-8588, Japan

[b] Department of Mechanical Systems Engineering, College of Engineering, Tokyo University of Agriculture and Technology, Tokyo, Japan

Received 15 December 2003; received in revised form 25 March 2004
Available online 19 May 2004

Abstract

Centrifugal buoyancy effect on heat transfer in a rotating two-pass rib-roughened channel with 180° sharp turns was numerically investigated by using the large eddy simulation. The effect of the aiding and opposing buoyancy contributions was seen in the suppressed turbulent transport in the radially inward flow, and in larger buoyancy-induced variation of the heat transfer on the pressure surface than that on the suction surface. As the buoyancy increased, the friction factor dominated by the pressure loss of the sharp turn decreased, and Colburn's j factor stayed almost constant. As a result, the heat transfer efficiency index slightly increased by the buoyancy, and it showed almost the same values among the three tested rib arrangements.

1. Introduction

The effective cooling of a gas turbine rotor blade is essential because the higher efficiency of the turbine requires a higher inlet gas temperature. Generally, this blade cooling is performed by film cooling at the external surface of the turbine blade and also by internal forced-convection cooling which uses winding flow passages inside the turbine blade. In the internal forced-convection cooling, the real phenomena are very complicated due to external forces: the Coriolis force and the buoyancy force in the centrifugal acceleration field. In addition to these external forces, the disturbances induced by turbulence promoters (ribs) and 180° sharp turns further complicate the phenomena [1].

As for the heat transfer in smooth and/or rib-roughened channels with the 180° sharp turn, several researchers investigated the detailed spatial variation of the local heat transfer in the stationary condition with various techniques: wall temperature measurement by using hundreds of thermocouples [2,3], naphthalene sublimation technique to measure the local mass transfer, which was transformed into heat transfer by using the analogy between heat and mass transfer [4,5], unsteady wall temperature measurement by using temperature-sensitive liquid crystal [6,7], and wall temperature measurement by using infrared thermography [8]. In these studies, the characteristic heat transfer variation induced by the ribs and the 180° sharp turn was captured: the high heat transfer areas observed in and after the sharp turn and on and between the ribs. As for the flow field in the stationary condition, Son et al. [9] applied the particle image velocimetry technique to the two-pass channel with the 180° sharp turn, and the detailed two-dimensional flow field was measured. For the rotating condition, however, both the flow velocity and

* Corresponding author. Tel.: +81-42-388-7089; fax: +81-42-385-7204.
E-mail address: murata@mmlab.mech.tuat.ac.jp (A. Murata).

0017-9310/$ - see front matter © 2004 Elsevier Ltd. All rights reserved.
doi:10.1016/j.ijheatmasstransfer.2004.03.025

Nomenclature

$A_{\text{total,nodim}}$ dimensionless total heat transfer area of channel
c_p specific heat, J/(kg K)
C_S Smagorinsky constant
C_θ coefficient of linear component in energy equation ($= A_{\text{total,nodim}}/32$)
D hydraulic diameter (= side length of straight-pass cross section), m
e height of rib, m
f friction factor ($= \Delta p_{\text{total}} D/(2\rho U_m^2 L)$)
F_i external force term
Gr_* Grashof number based on friction temperature ($= \beta T_r \omega^2 R_{m,\text{dim}} \ell^3/\nu^2$)
$Gr_{m,q}$ Grashof number based on wall heat flux ($= \beta \dot{q} \omega^2 R_{m,\text{dim}} D^4/(\nu^2 \lambda)$)
$Gr_{m,\Delta T}$ Grashof number based on temperature difference ($= \beta \Delta T \omega^2 R_{m,\text{dim}} D^3/\nu^2$)
h heat transfer coefficient, W/(m^{2}K)
H_0 dimensionless distance between rotation axis and x axis ($= H_{0,\text{dim}}/\ell$)
$H_{0,\text{dim}}$ distance between rotation axis and x axis ($z = 0$), m
j Colburn's j factor ($= Nu_m/(Re_m Pr^{1/3})$)
k dimensionless turbulent kinetic energy
K_{straight} pressure loss coefficient of straight pass $\left(= \Delta p_{\text{straight}}/\left(\frac{1}{2}\rho U_m^2\right)\right)$
K_{turn} pressure loss coefficient of sharp turn $\left(= \Delta p_{\text{turn}}/\left(\frac{1}{2}\rho U_m^2\right)\right)$
ℓ length scale ($= 0.5D$), m
L total duct-axial length of two-pass channel ($= 22D$), m
Nu Nusselt number ($= hD/\lambda$)
P rib pitch ($= D$), m
$\Delta p_{\text{straight}}$ pressure loss at straight pass, Pa
Δp_{total} pressure loss between channel inlet and outlet, Pa
Δp_{turn} pressure loss between turn inlet and outlet, Pa
Pr Prandtl number ($= 0.71$)
Pr_{SGS} Prandtl number of subgrid-scale model ($= 0.5$)
$\dot{q}$ wall heat flux, W/m^2
Q second invariant of deformation tensor
R_m dimensionless mean rotation radius ($= R_{m,\text{dim}}/\ell$)
$R_{m,\text{dim}}$ mean rotation radius, m
Ra_* Rayleigh number ($= Gr_* Pr$)
Re_m Reynolds number based on bulk mean velocity ($= U_m D/\nu$)
Re_* Reynolds number based on friction velocity ($= u_* \ell/\nu$)
Ro_m rotation number based on bulk mean velocity ($= \omega D/U_m$)
Ro_* rotation number based on friction velocity ($= \omega \ell/u_*$)
S_{ij} rate-of-strain tensor
St Stanton number ($= Nu_m/(Re_m Pr)$)
t dimensionless time
ΔT mean temperature difference between wall and fluid ($= (T_w - T_b)_m$), K
T temperature, K
T_{linear} linearly increasing component of temperature, K
T_r friction temperature ($= \dot{q}/(\rho c_p u_*)$), K
u,v,w dimensionless velocities in x, y, z directions
u_* mean friction velocity calculated from mean pressure gradient in x direction, m/s
$u_{*\text{mod}}$ mean friction velocity estimated by using bulk mean velocity, m/s
$\bar{u}_m$ dimensionless bulk mean velocity in x direction calculated at the entrance $\left(= \frac{1}{4}\int_{-1}^{1}\int_{-1}^{1} \bar{u}_{x=0}\,dy\,dz\right)$
U_m bulk mean velocity, m/s
x,y,z dimensionless Cartesian coordinates
$\alpha_{\text{SGS}j}$ subgrid-scale energy flux
β expansion coefficient, 1/K
$\Delta_1,\Delta_2,\Delta_3$ grid spacing in ξ, η, ζ directions expressed in (x, y, z) coordinates' scale
η_{eff} heat transfer efficiency index ($= (St/St_{\text{smooth,stationary}})/(f/f_{\text{smooth,stationary}})^{1/3}$)
λ thermal conductivity, W/(m K)
ν kinematic viscosity, m^2/s
ν_{SGS} dimensionless subgrid-scale eddy viscosity
ω angular velocity, rad/s
ρ density, kg/m^3
θ dimensionless temperature ($= (T - T_{\text{linear}})/T_r$)
$\tau_{\text{SGS}ij}$ subgrid-scale stress tensor
$\tau_{w,s}$ streamwise component of wall shear stress, Pa
ξ,η,ζ curvilinear coordinates

Subscripts and superscripts

b bulk value
B Blasius
L local value
m duct average or based on bulk mean velocity
w wall
∞ fully developed
* friction velocity or defined by using u_*
+ dimensionless value based on inner scales
− grid resolvable component

wall temperature measurements become very difficult because of the following two reasons: the high centrifugal force preventing the data acquisition system from normal operation and the difficulty in transferring data from the rotating system to the stationary system. Nevertheless, some researchers have performed experiments in the rotating condition by measuring the wall temperature distribution using thermocouples for the smooth [10–12] and rib-roughened [13–15] wall two-pass channels with the 180° sharp turn. Liou et al. [16] conducted the flow velocity measurement of a rotating two-pass smooth channel with the 180° sharp turn by using the laser Doppler anemometer in addition to the detailed heat transfer measurement by using the transient liquid crystal method. However, it is extremely difficult to perform the experiments in the rotating condition that can identify both the flow structure and its influence on the heat transfer at the same time. Thus, further progress in experimental studies has so far been prevented.

In previous numerical studies of the serpentine flow passage with the 180° sharp turn, the Reynolds-averaged Navier–Stokes equation with a turbulence model was adopted: Banhoff et al. [17] used the k–ε two-equation turbulence model or the Reynolds stress equation model with the wall function, and Lin et al. [18] used the low-Reynolds number two-equation turbulence model without the wall function. Although this approach using the Reynolds-averaged turbulence model could reproduce the heat transfer of blade cooling to a certain extent, even the Reynolds stress equation model has empirical constants and functions, and therefore the applicability of the model should carefully be examined. Recent advancement in computers enables us to numerically simulate the fluctuating components of the turbulent flow by using the large eddy simulation (LES) or the direct numerical simulation (DNS), and the techniques were applied to the smooth straight duct in the stationary [19–21] and rotating [22,23] conditions. Because LES and DNS directly resolve temporal variation of the fluctuating components, the results are more universal, in other words, more free from the empirical modeling than the Reynolds-averaged turbulence models. Although LES also has empirical constants and functions, the modeling of the turbulence is confined to the subgrid-scale turbulence, and therefore the effect of the empirical modeling on the result is ideally less than that in the Reynolds stress equation model. Recently, the authors performed the numerical analyses by using a dynamic subgrid-scale model for a rotating angled-rib-roughened straight duct [24,25], and for the two-pass smooth [26] and rib-roughened [27] channels with the 180° sharp turn in the stationary and rotating conditions. The effect of the buoyancy force in the centrifugal acceleration field is very important considering the highly severe thermal condition with high rotation rate to which the real turbine blades are exposed. The buoyancy effect was examined for smooth and rib-roughened straight duct cases in [25], and for the two-pass smooth channel in [28] where the aiding and opposing contributions of the centrifugal buoyancy was clarified. However, so far the buoyancy effect in the two-pass rib-roughened channel with the sharp turn has not been investigated yet by using either LES or DNS.

This study examines how the centrifugal buoyancy force affects the heat transfer in the rotating two-pass rib-roughened channel with 180° sharp turns. The computations were performed varying the Rayleigh number for three different rib arrangements: a 90° transverse rib and two different angled 60° rib arrangements. The attention was paid to the relation between the main flow and centrifugal buoyancy force directions, because the radially outward and inward flow cases became different when the centrifugal buoyancy was introduced.

2. Numerical analysis

Fig. 1 shows the computational domain and coordinate system used in this study. The duct had a square cross section with a side length of D. The coordinate system was fixed to a rotating channel that had an angular velocity of ω with respect to the axis of rotation parallel to the x-axis. The axial direction of the channel straight pass was parallel to the z direction; the x and y directions were the parallel and perpendicular directions, respectively, to leading/trailing walls. The inner and outer walls at the turn A was named the inner and outer walls, respectively. Therefore, it should be noted that "inner wall" and "outer wall" of this study came to the outer and inner sides at the turn B, respectively, unless otherwise mentioned. Round-type ribs as used in [17,18] were installed with the in-line arrangement on the trailing and leading walls with the rib angle of 90° or 60° with respect to duct axis of the straight pass. As shown in Fig. 1, the cross section of the round-type rib was composed of the quadrants of which radius was $0.05D$, and thus the rib height was $e = 0.1D$. The streamwise rib-pitch, P, was set equal to the hydraulic diameter, D. This rib arrangement gave the rib height-to-hydraulic diameter ratio $e/D = 0.1$ and the rib pitch-to-rib height ratio $P/e = 10$. This rib arrangement was chosen because it was within the previously reported optimal range for straight ducts considering both the Nusselt number and the friction factor [29–31]. The rib angle, 60°, was chosen as the angle which gave the maximum heat transfer for straight ducts in Han et al. [32]. As shown in Fig. 2, three rib arrangements were investigated in this study: a 90° rib arrangement and two 60° rib arrangements. For the 60° rib "NP" and "PN" arrangements, "N" and "P" were from "Negative" and "Positive" considering relation between angled-rib

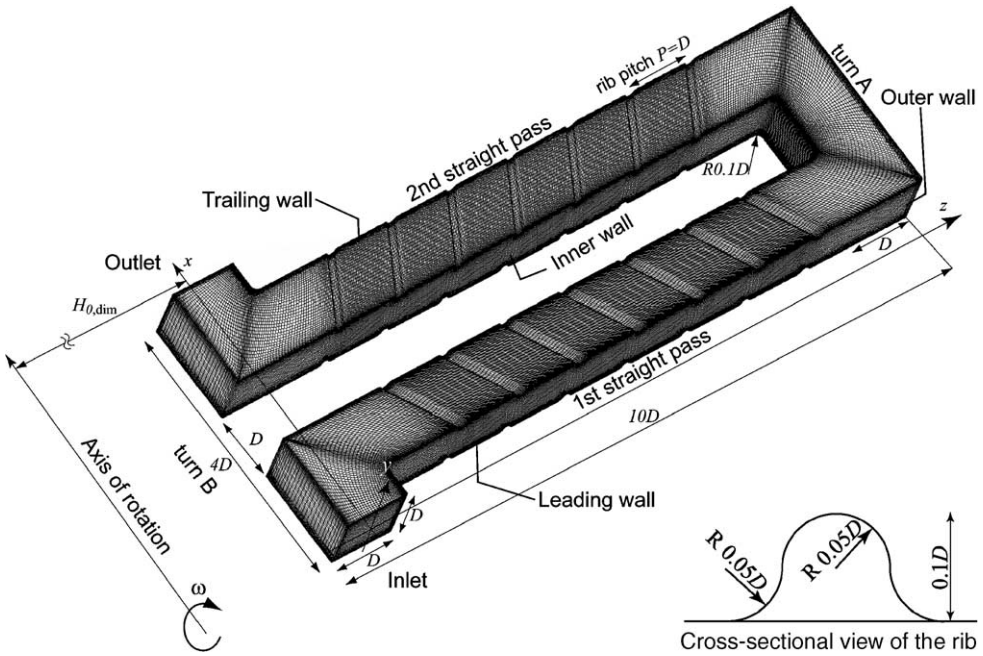

Fig. 1. Schematic of a rotating two-pass rib-roughened square channel with sharp 180° turns (60° rib with NP arrangement is shown).

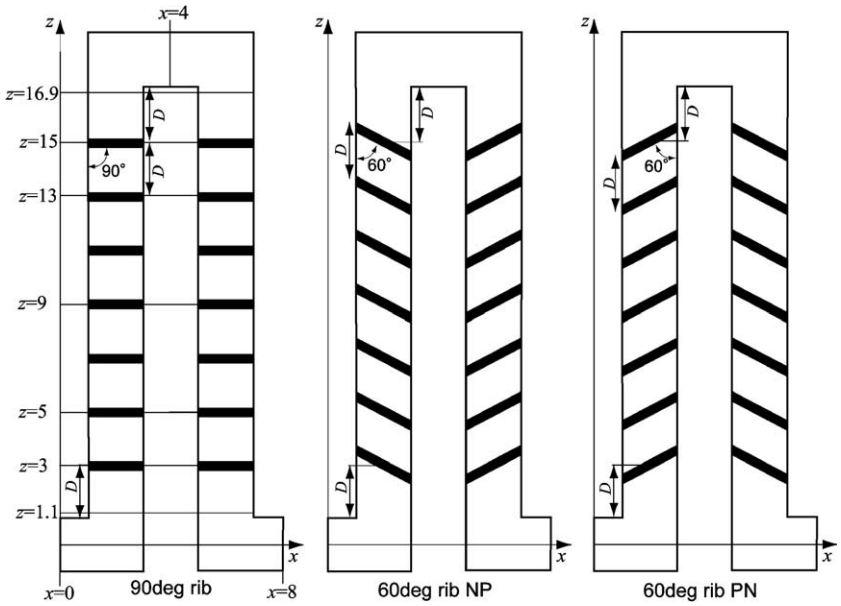

Fig. 2. Rib arrangements of this study (all cases are in-line arrangement).

induced and sharp-turn induced secondary flow directions. For example, in the "PN" arrangement the angled-rib induced secondary flow in the first straight pass circulated in the same direction as the turn A induced one, and on the other hand that in the second straight pass circulated in the opposite direction to the turn A induced one.

The present procedure of the numerical analysis was the same as our recent studies [26–28]. After applying a filtering operation to the incompressible

Navier–Stokes equation with a filter width equal to the grid spacing [21], the dimensionless governing equations scaled by a length scale, ℓ ($= 0.5D$), and a mean friction velocity, u_*, became a set of dimensionless governing equations with respect to grid resolvable components indicated by overbars as $(\bar{u}, \bar{v}, \bar{w})$ under the assumption of constant fluid properties. In order to simulate a fully developed situation, the pressure and temperature fields were decomposed into the steady and x-directional linear component and the remaining component [33]. By this decomposition, the latter component of the pressure and temperature fields can be treated using a periodic boundary condition in the x direction.

The temperature was made dimensionless by using a linearly increasing component of temperature, T_{linear}, and a friction temperature, T_r, as $\theta = (T - T_{\text{linear}})/T_r$. Accordingly, the dimensionless energy equation was derived for the grid resolvable component, $\bar{\theta}$. The governing equations in the Cartesian coordinates (x, y, z) were transformed into generalized curvilinear coordinates (ξ, η, ζ) that were aligned to the structured grid coordinate of this study: ζ was the duct-axial direction. The governing equations in the curvilinear coordinate system were expressed as follows [34]:

$$\frac{1}{J}\frac{\partial J\overline{U}^j}{\partial \xi^j} = 0, \tag{1}$$

$$\frac{\partial \bar{u}_i}{\partial t} = -\overline{U}^j \frac{\partial \bar{u}_i}{\partial \xi^j} - \frac{\partial \xi^j}{\partial x_i}\frac{\partial \bar{p}}{\partial \xi^j} + \frac{1}{Re_*}\frac{\partial \xi^j}{\partial x_\ell}\frac{\partial}{\partial \xi^j}\left(\frac{\partial \xi^k}{\partial x_\ell}\frac{\partial \bar{u}_i}{\partial \xi^k}\right) + \frac{\partial \xi^k}{\partial x_j}\frac{\partial \tau_{\text{SGS}ij}}{\partial \xi^k} + F_i, \tag{2}$$

$$\frac{\partial \bar{\theta}}{\partial t} = -\overline{U}^j \frac{\partial \bar{\theta}}{\partial \xi^j} - C_\theta \frac{\bar{u}}{\bar{u}_{\text{m}}} + \frac{1}{Re_* Pr}\frac{\partial \xi^j}{\partial x_\ell}\frac{\partial}{\partial \xi^j}\left(\frac{\partial \xi^k}{\partial x_\ell}\frac{\partial \bar{\theta}}{\partial \xi^k}\right) + \frac{\partial \xi^k}{\partial x_j}\frac{\partial \alpha_{\text{SGS}j}}{\partial \xi^k}, \tag{3}$$

where $\overline{U}^j$ was a contravariant component of velocity, and the following expressions were assumed: $J = \partial(x, y, z)/\partial(\xi, \eta, \zeta)$, $(x_1, x_2, x_3) = (x, y, z)$, and $(\xi^1, \xi^2, \xi^3) = (\xi, \eta, \zeta)$.

An external force term, F_i, in the momentum equations (Eq. (2)) had the Coriolis force, the centrifugal buoyancy force with the Boussinesq approximation, and the mean pressure gradient term with a value of 2 as shown in the following equation:

$$F_i = \begin{pmatrix} 2 \\ 2Ro_*\bar{w} - \dfrac{Gr_*}{Re_*^2}\dfrac{(\bar{\theta} - \bar{\theta}_\infty)y}{R_{\text{m}}} \\ -2Ro_*\bar{v} - \dfrac{Gr_*}{Re_*^2}\dfrac{(\bar{\theta} - \bar{\theta}_\infty)}{R_{\text{m}}}(H_0 + z) \end{pmatrix}. \tag{4}$$

Because the dimensionless mean rotation radius, R_{m}, is much larger than y and z in the real gas turbines, the following approximation can be used: $y/R_{\text{m}} \fallingdotseq 0$ and $(H_0 + z)/R_{\text{m}} \fallingdotseq 1$. In the dimensionless reference temperature of $\theta_\infty = (T_\infty - T_{\text{linear}})/T_r$, T_{linear} changes linearly in the x direction, and therefore $\bar{\theta}_\infty$ also changes linearly in the x direction. From the energy balance, the following equation holds:

$$\bar{\theta}_\infty = -C_\theta \frac{x}{\bar{u}_{\text{m}}}. \tag{5}$$

Consequently Eq. (4) was approximated as follows:

$$F_i = \begin{pmatrix} 2 \\ 2Ro_*\bar{w} \\ -2Ro_*\bar{v} - \dfrac{Gr_*}{Re_*^2}(\bar{\theta} - \bar{\theta}_\infty) \end{pmatrix}. \tag{6}$$

In this study, the friction velocity, u_*, was calculated from the force balance between the mean pressure gradient in the x direction and the wall shear stress as follows:

$$\rho u_*^2 = \frac{\ell}{2}\left|\frac{\mathrm{d}p}{\mathrm{d}x}\right|_{\text{m,dim}}. \tag{7}$$

Here, the mean pressure gradient with the subscript, "dim", meant the value with dimension, and it drove the flow in the x direction. By non-dimensionalizing equation (7), the dimensionless mean pressure gradient value of 2 came out. Because of the constant mean pressure gradient, the flow rate varied depending on the Rayleigh number and the rib arrangement; therefore, the flow rate was not known a priori, and it was calculated from the resultant computed flow field after the fully developed condition was attained. In this study, the fully developed condition was judged by the statistical steadiness.

Subgrid-scale components of stress, $\tau_{\text{SGS}ij}$, and energy flux, $\alpha_{\text{SGS}j}$, were expressed as follows:

$$\tau_{\text{SGS}ij} = 2\nu_{\text{SGS}}\overline{S}_{ij}, \tag{8}$$

$$\alpha_{\text{SGS}j} = \frac{\nu_{\text{SGS}}}{Pr_{\text{SGS}}}\frac{\partial \xi^k}{\partial x_j}\frac{\partial \bar{\theta}}{\partial \xi^k}, \tag{9}$$

where

$$\overline{S}_{ij} = \frac{1}{2}\left(\frac{\partial \xi^k}{\partial x_j}\frac{\partial \bar{u}_i}{\partial \xi^k} + \frac{\partial \xi^k}{\partial x_i}\frac{\partial \bar{u}_j}{\partial \xi^k}\right), \tag{10}$$

$$\nu_{\text{SGS}} = C_S^2(\Delta_1\Delta_2\Delta_3)^{2/3}\sqrt{2\overline{S}_{ij}\overline{S}_{ij}}. \tag{11}$$

Because the flow field of this study has no homogeneous direction, we adopted the Lagrangian dynamic subgrid-scale model of Meneveau et al. [35] that averaged the value of C_{S} along the path-line for a certain distance. As for the coefficient of the Lagrangian averaging time scale, the same value of 1.5 as that in [35] was used. The

turbulent Prandtl number for the subgrid-scale component, Pr_{SGS}, was set to 0.5 [36]. These values were mainly tested for the two-dimensional channel turbulence, and therefore there may be room for further optimization of them to the present complicated flow passage. However, we adopted the above-mentioned values considering the fact that the results in [35] showed acceptably small sensitivity to the coefficient of the Lagrangian averaging time scale, and the value of Pr_{SGS} also showed small sensitivity to the flow types and grid resolution in [36]. The width of the test filter was double the grid spacing.

Discretization was performed by a finite difference method using the collocated grid system [34]. The spatial and temporal discretization schemes were similar to those of Gavrilakis [20]: the second order central differencing method and the Crank–Nicolson method for the viscous term, and the second order differencing method satisfying the conservative property [34] and the second order Adams-Bashforth method for the convective term. The external force term was also treated by the second order Adams-Bashforth method. The pressure field was treated following the MAC method [37]. At the wall boundary, no-slip and constant heat flux conditions were imposed. The boundary conditions of the intermediate velocities and pressure were set following the procedure of [38,39].

The local Nusselt number, Nu_L, was calculated from the wall temperature as follows:

$$Nu_L = \frac{2Re_*Pr}{\bar{\theta}_w - \bar{\theta}_b}. \tag{12}$$

The averaged Nusselt number was calculated by using the integrally averaged temperature difference for the area in question.

In this study, the values of Re_* $(= u_*\ell/v)$ and Ro_* $(= \omega\ell/u_*)$ were maintained at $(Re_*, Ro_*) = (1000, 1)$, and the Rayleigh number, Ra_*, was varied among 0 to 2×10^4. In correlating the experimental results, the effect of the buoyancy is often expressed by using the Grashof number, $Gr_{m,q}$, which is defined with the wall heat flux. The following relation holds due to the definition of $Gr_{m,q}$:

$$Gr_{m,q} = 16Re_*PrGr_* = 16Re_*Ra_*. \tag{13}$$

The conversion of the dimensionless numbers of this study (Re_*, Ro_*, Ra_*) defined by the mean friction velocity, the friction temperature, and the length scale of $0.5D$ into those of $(Re_m, Ro_m, Gr_{m,q})$ defined by the bulk mean velocity, the wall heat flux, and the hydraulic diameter, D, was summarized in Table 1. In Table 1, our previous numerical results for the smooth two-pass channel [28] are also included for comparison. In the real aircraft gas turbine engines, the central region of the operating range is in the order of $Re_m \sim 10^4$, $Ro_m \sim 10^{-1}$, and $Gr_{m,\Delta T}/Re_m^2 \sim 10^{-1}$ [11]. From the definition of Grashof numbers, the following relation holds between $Gr_{m,q}$ and $Gr_{m,\Delta T}$:

Table 1
Dimensionless number range of this study and the duct averaged values of f and Nu_m

Rib arrangement	Re_*	Ro_*	Ra_*	Re_m	Ro_m	$Gr_{m,q}$	$\frac{Gr_{m,q}}{Re_m^2}$	$\frac{Gr_{m,\Delta T}}{Re_m^2}$	f/f_B	Nu_m/Nu_∞ $(= j/j_\infty)$
90°	1000	1	0	3339	1.20	0	0	0	12.55	2.62
			5×10^3	3787	1.06	8.0×10^7	5.58	0.15	10.07	2.66
			1×10^4	4194	0.95	1.6×10^8	9.10	0.23	8.43	2.66
			2×10^4	4687	0.85	3.2×10^8	14.57	0.34	6.94	2.67
60° NP	1000	1	0	3447	1.16	0	0	0	11.87	2.67
				(3501)	(1.14)				(11.56)	(2.70)
			5×10^3	3900	1.03	8.0×10^7	5.26	0.14	9.57	2.66
			1×10^4	4237	0.94	1.6×10^8	8.91	0.22	8.28	2.69
			2×10^4	4779	0.84	3.2×10^8	14.01	0.32	6.70	2.68
				(4736)	(0.84)				(6.81)	(2.72)
60° PN	1000	1	0	3437	1.16	0	0	0	11.94	2.68
			5×10^3	3889	1.03	8.0×10^7	5.29	0.14	9.61	2.71
			1×10^4	4218	0.95	1.6×10^8	8.99	0.22	8.34	2.75
			2×10^4	4672	0.86	3.2×10^8	14.66	0.34	6.97	2.73
Smooth [28]	1000	1	0	4028	0.99	0	0	0	9.04	2.39
				(4150)	(0.96)				(8.58)	(2.37)
			5×10^3	4199	0.95	8.0×10^7	4.54	0.13	8.41	2.40
			1×10^4	4563	0.88	1.6×10^8	7.68	0.21	7.27	2.38
			2×10^4	5059	0.79	3.2×10^8	12.50	0.31	6.07	2.37

The values in parentheses in the second line are for higher grid resolution of $71\times71\times965$ with reduced sample size of 50,000 steps. The smooth channel data are from Murata and Mochizuki [28].

$$Gr_{m,q} = Nu_m Gr_{m,\Delta T}. \quad (14)$$

Note that as compared to the real situation the computational conditions of this study are smaller for Re_m because of the limited grid resolution. The buoyancy parameter [11], $Gr_{m,\Delta T}/Re_m^2$, of this study is in the same order of the real situation (see Table 1).

As shown in Fig. 1, the structured grid system was generated by using Gridgen Ver.14 (Pointwise Inc.). The grids in the physical domain were contracted to the walls and the corners. On the rib-roughened surfaces, the grids were aligned to the ribs. The grid number was mainly $47\times47\times965$ in ξ, η, ζ directions, and this grid configuration, for example, gave a grid spacing of $\Delta_1^+ = 0.42$–18.4, $\Delta_2^+ = 0.55$–13.3, and $\Delta_3^+ = 1.6$–23.5 ($Ro_* = 1$ and $Ra_* = 2\times10^4$) for the 60° rib NP case. Here, the inner length scale of $v/u_{*\mathrm{mod}}$ was used, because the friction velocity, u_*, defined in Eq. (7) overestimated the value. In Eq. (7), the streamwise direction was assumed to be only in the x direction, and therefore it cannot account for the longer total flow distance caused by the change of the streamwise direction in the two-pass channel. In order to estimate appropriate inner length and time scales, the friction velocity, $u_{*\mathrm{mod}}$, was calculated by using the resultant flow rate for each condition and the Blasius equation. The effect of the grid spacing on the computed result was checked by increasing the grid number to $71\times71\times965$ for several cases, and no major difference was observed as shown in Table 1. The time step interval was $\Delta t = 1.0\times10^{-4}$, which can be expressed as $\Delta t^+ = 0.016$ when made dimensionless by an inner time scale, $v/u_{*\mathrm{mod}}^2$ for the 60° rib NP case ($Ro_* = 1$ and $Ra_* = 2\times10^4$).

In order to deal with the very high computational load of this study, the computational domain was decomposed into 64 sub-domains in the duct-axial (ζ) direction, and the parallel computing technique was applied. Each sub-domain's computation was performed on a different CPU on HITACHI SR8000/MPP (Information Technology Center, The University of Tokyo). When the algebraic equation for each variable was solved by using the SOR method, the values at the sub-domain boundaries were transferred to the neighboring sub-domains by using MPI functions in each iteration step.

The computation was started using the result of the similar condition as an initial condition. At first, the calculations were carried out till the statistically steady flow condition was attained. After that, additional 90,000 steps ($t = 9$ or $t^+ = 1440$ for 60° rib NP case ($Ro_* = 1$ and $Ra_* = 2\times10^4$)) were performed for computing the statistical values. This 90,000 step computation needed about 11.5×64 CPU hours for the $47\times47\times965$ grid configuration.

3. Results and discussion

At first, the verification of the present numerical procedure is explained. In our previous studies of smooth [26] and rib-roughened [27] two-pass channels, the numerical results were compared with the experimental results of the stationary condition in the local and transversely averaged Nusselt numbers and also in the channel averaged f and j factors. The agreement between the numerical and experimental results was good, and the present numerical procedure was able to reproduce the heat transfer enhancement in and after the sharp turn and the quick development of the saw-toothed-profile heat transfer augmentation due to the periodically installed ribs in the straight pass [26,27].

Figs. 3–8 show the local Nusselt number (Figs. (a)) and the streamwise component of the wall shear stress (Figs. (b)) on all four walls by viewing the flow channel from six different directions. Figs. 3, 5 and 7 are without buoyancy ($Ra_* = 0$), and Figs. 4, 6 and 8 are with buoyancy ($Ra_* = 2\times10^4$). The Nusselt number of this study was normalized using the following empirical correlation for a fully developed pipe flow [40]:

$$Nu_\infty = 0.022 Re_m^{0.8} Pr^{0.5}. \quad (15)$$

It should be noted that the lower part of "Outer wall" in the figure shows the inner wall values because it is visible through the inlet and outlet of the channel. In Figs. (b), zero shear stress boundary is indicated by a white line. In the calculation of the streamwise component of the wall share stress, the streamwise direction was approximated by the ζ direction. In this study, the trailing and leading walls of the first straight pass correspond to the pressure and suction surfaces, respectively, and opposite relation holds in the second straight pass. The pressure and suction surfaces are defined with respect to the secondary flow induced by the Coriolis force, which impinges onto the pressure surface. Without the buoyancy ($Ra_* = 0$), in all the three rib arrangements of the 90° rib (Fig. 3), the 60° rib NP (Fig. 5), and the 60° rib PN (Fig. 7), the following characteristics are common. In the turn A, the high heat transfer area on the leading wall is intensified at the turn central area, and that on the trailing wall is separated in two regions: around the first inner corner and the second outer corner. The high Nusselt number area on the outer wall in the turn is slightly shifted to the trailing wall side. On the rib-roughened pressure surfaces, the profile becomes periodic in the streamwise direction due to the periodic installation of the ribs: the flow separation and its reattachment occur between the ribs, and the heat transfer is high on the rib surface and near the flow reattachment location. When the pressure and suction surfaces are compared, the intensified reverse flow area on the suction surface is

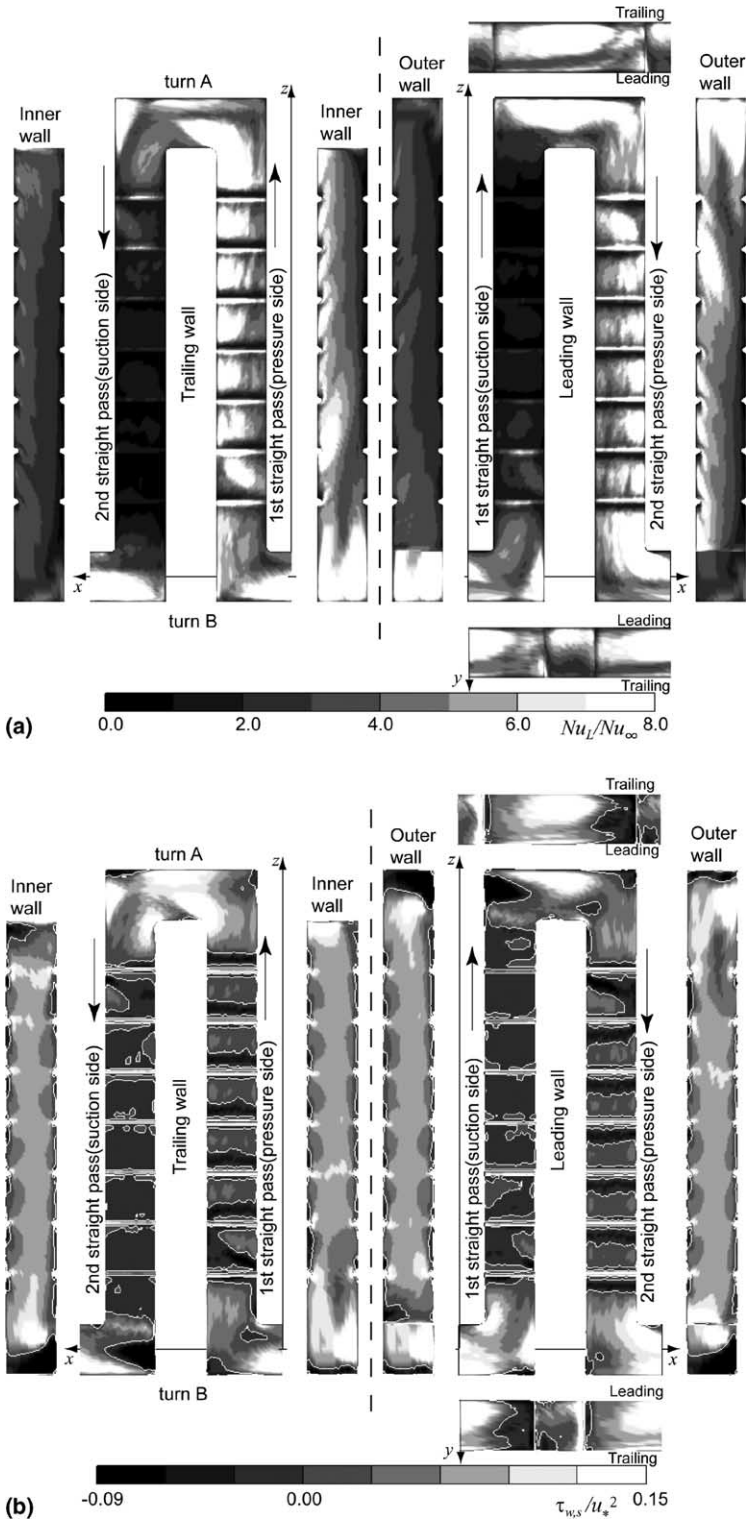

Fig. 3. Time-averaged profiles of (a) Nusselt number and (b) streamwise component of wall shear stress (90° rib, $Re_* = 1000$, $Ro_* = 1$, and $Ra_* = 0$).

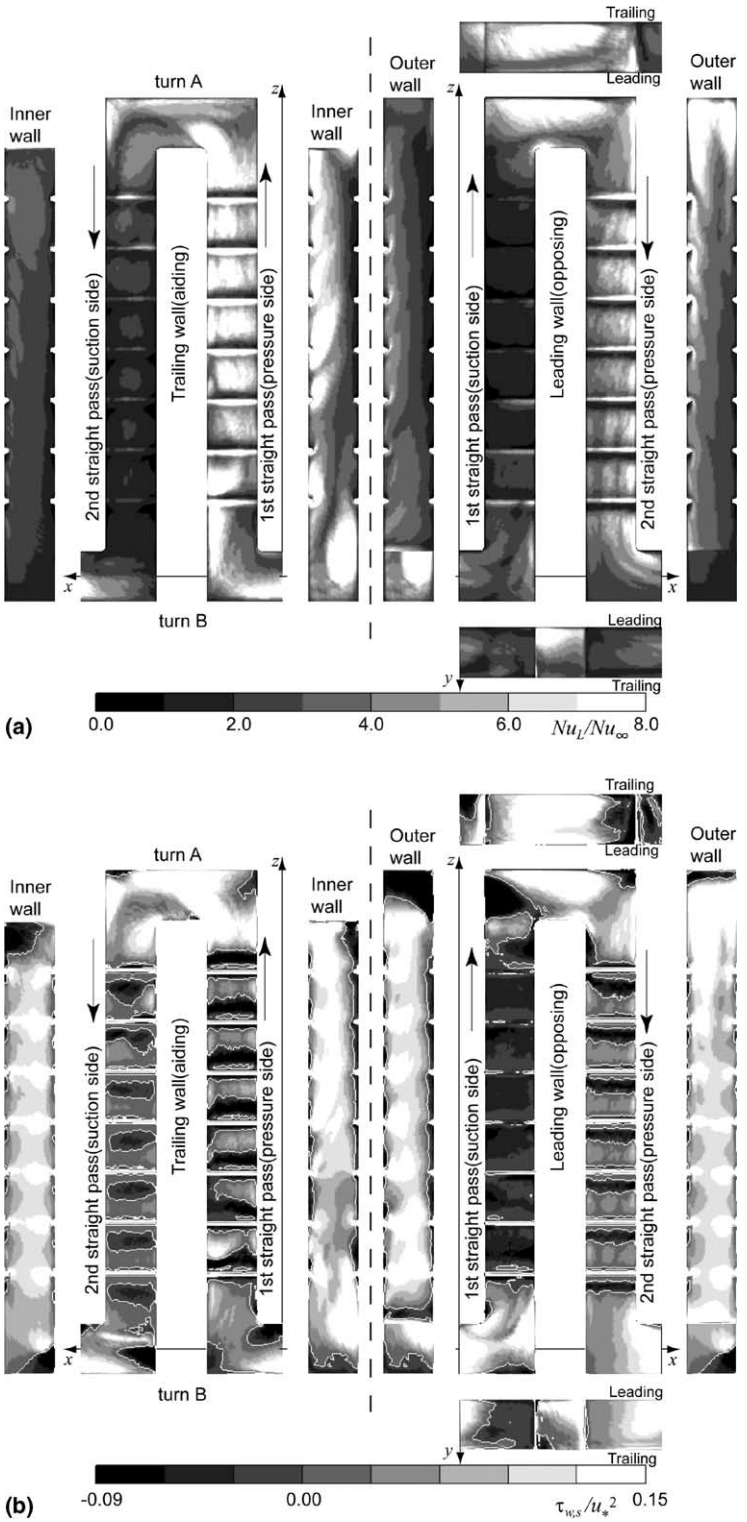

Fig. 4. Time-averaged profiles of (a) Nusselt number and (b) streamwise component of wall shear stress (90° rib, $Re_* = 1000$, $Ro_* = 1$, and $Ra_* = 2 \times 10^4$).

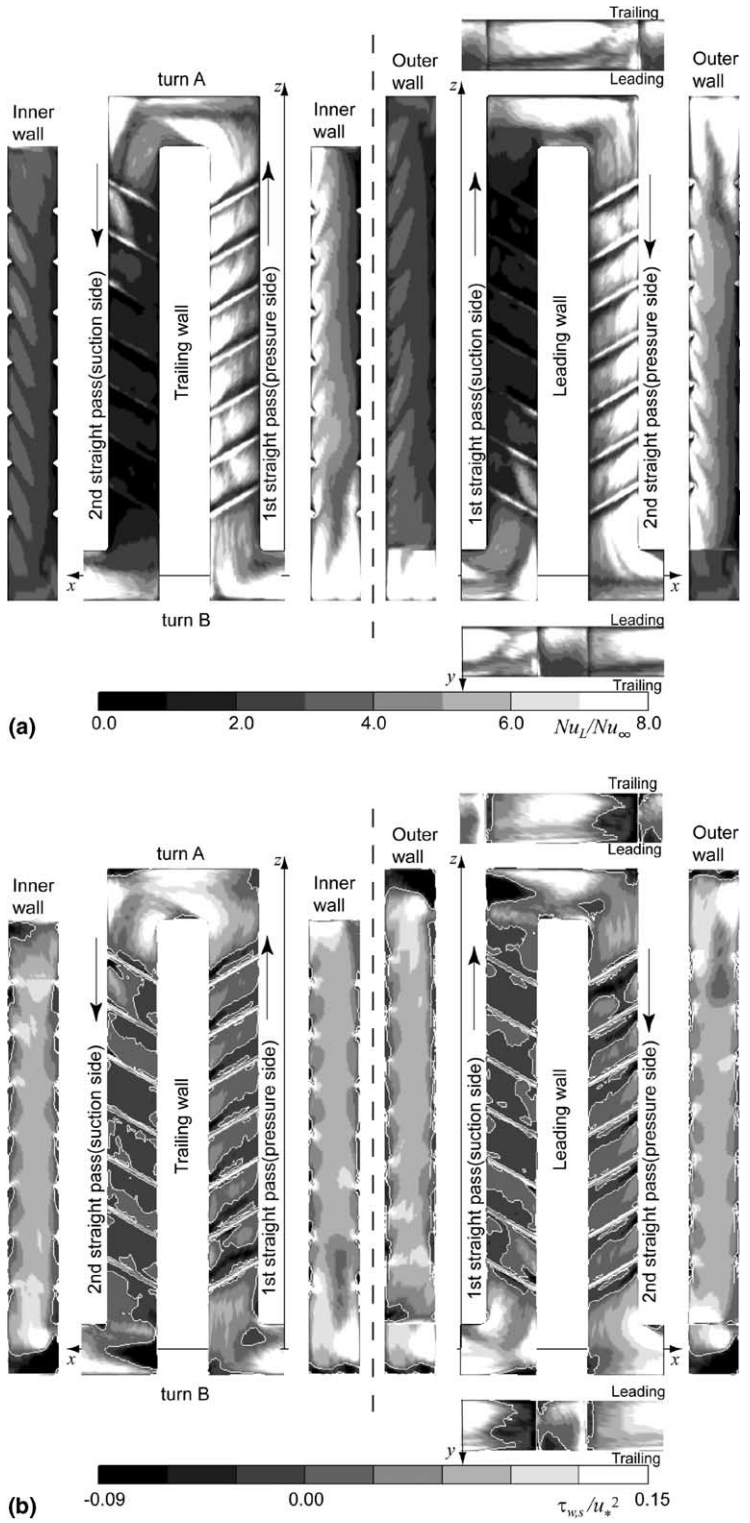

Fig. 5. Time-averaged profiles of (a) Nusselt number and (b) streamwise component of wall shear stress (60° rib NP, $Re_* = 1000$, $Ro_* = 1$, and $Ra_* = 0$).

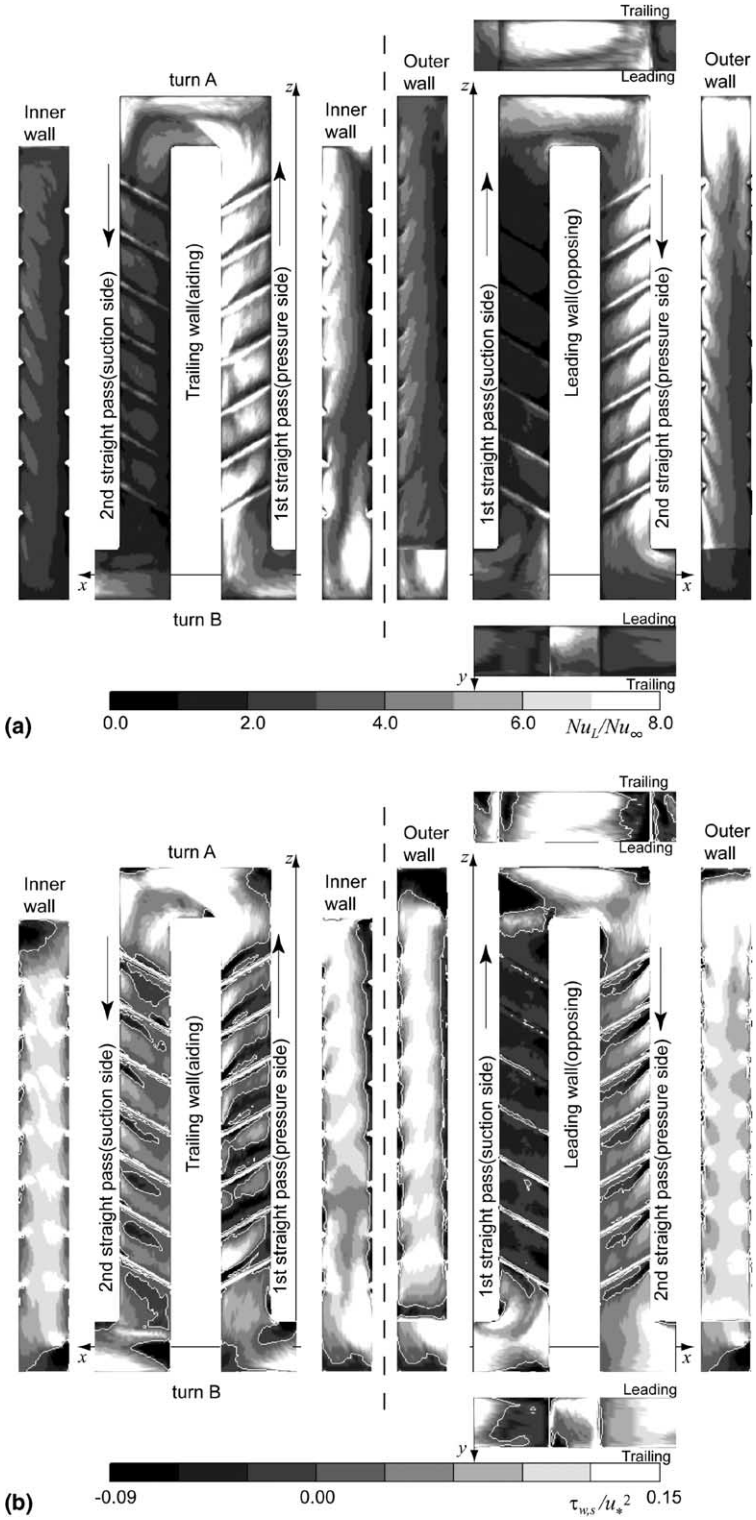

Fig. 6. Time-averaged profiles of (a) Nusselt number and (b) streamwise component of wall shear stress (60° rib NP, $Re_* = 1000$, $Ro_* = 1$, and $Ra_* = 2 \times 10^4$).

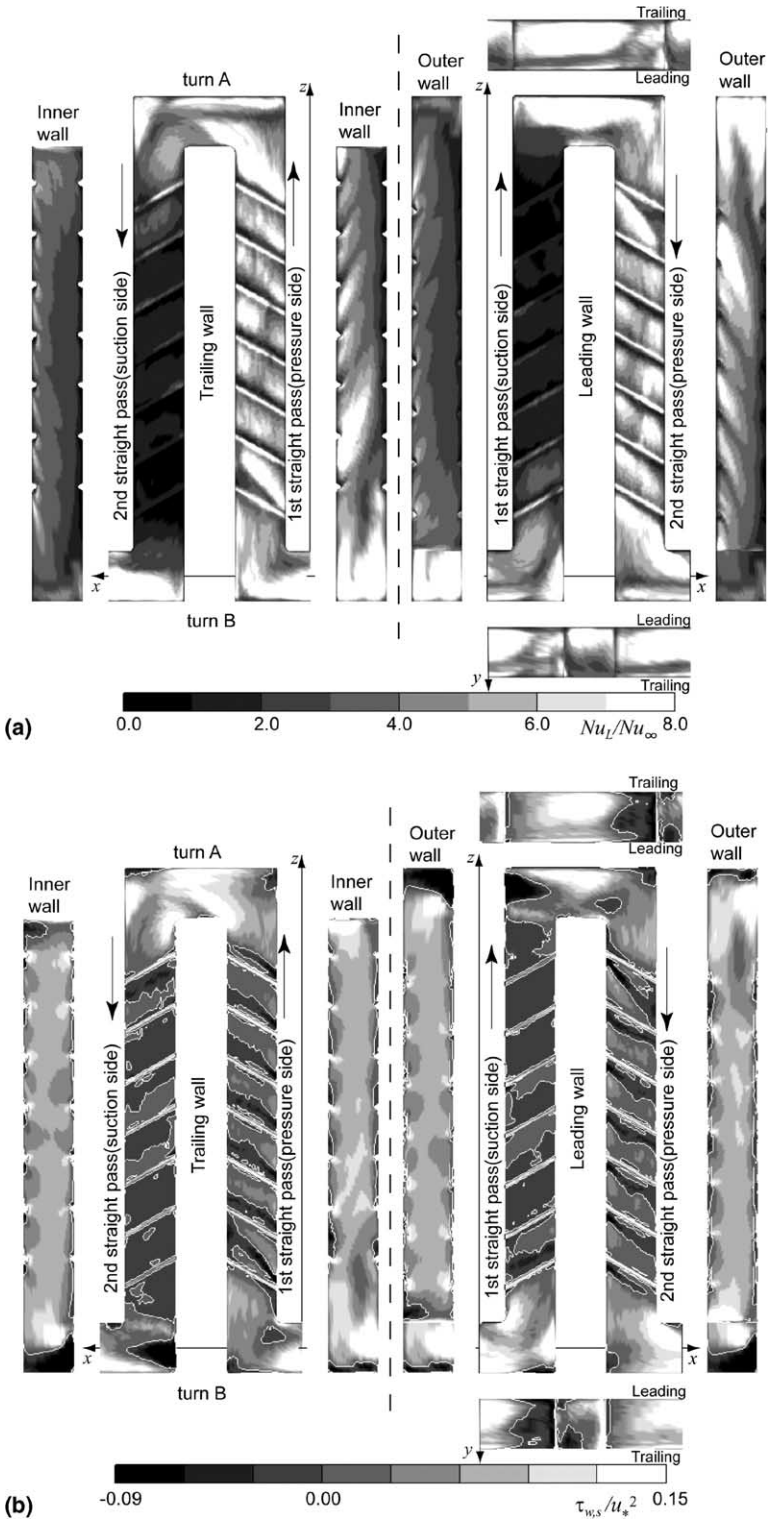

Fig. 7. Time-averaged profiles of (a) Nusselt number and (b) streamwise component of wall shear stress (60° rib PN, $Re_* = 1000$, $Ro_* = 1$, and $Ra_* = 0$).

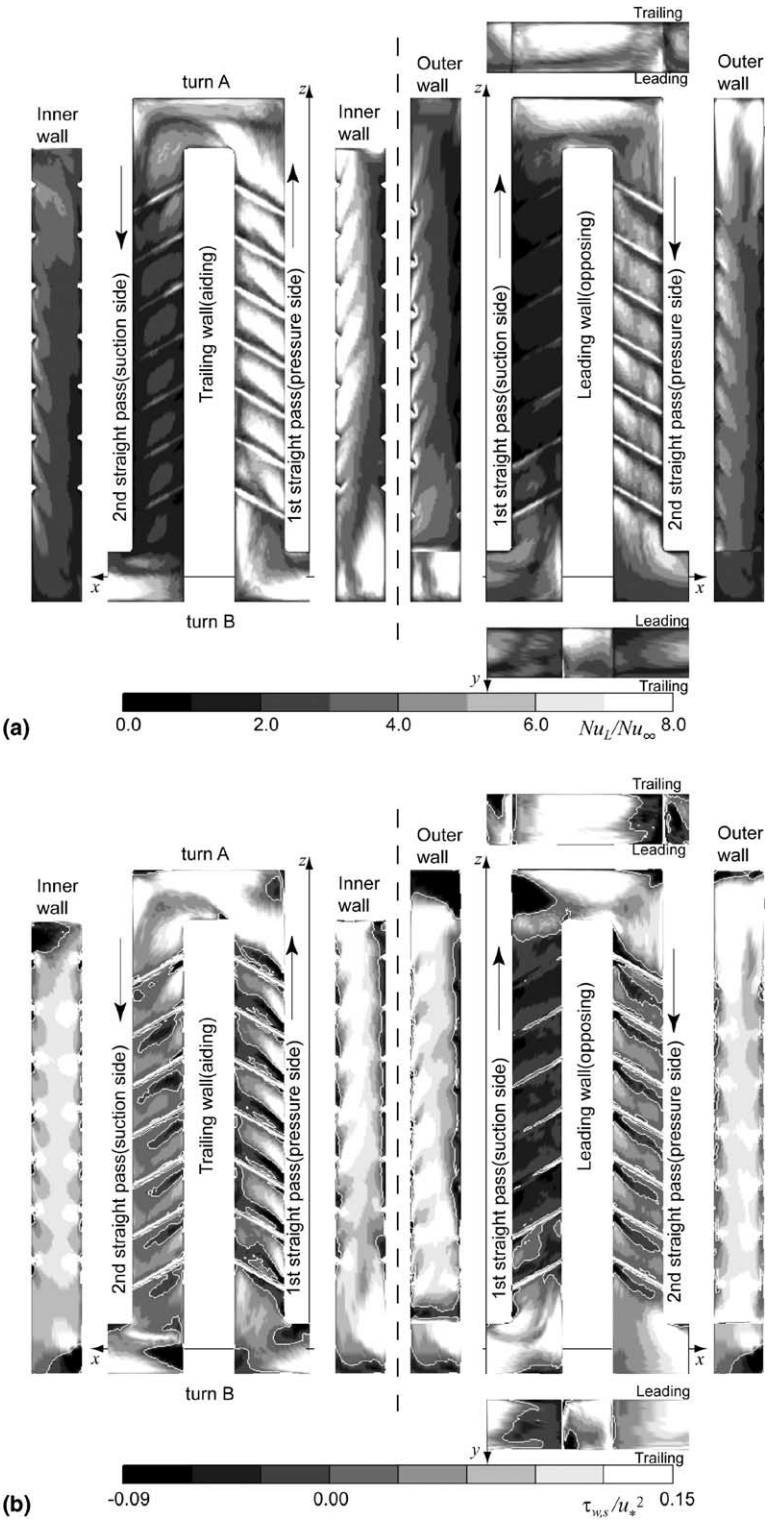

Fig. 8. Time-averaged profiles of (a) Nusselt number and (b) streamwise component of wall shear stress (60° rib PN, $Re_* = 1000$, $Ro_* = 1$, and $Ra_* = 2 \times 10^4$).

recognized by the extended area of the negative wall shear stress between the ribs, and the heat transfer on the suction surface is much lower than that on the pressure surface.

As discussed in [28], because of the secondary flow induced by the Coriolis force, the fluid temperature on the trailing (pressure) side of the first straight pass becomes lower than that on the leading (suction) side; therefore, on the pressure and suction surfaces of the first straight pass (radially outward flow), the buoyancy works in the aiding and opposing directions to the main flow, respectively (see Fig. 9(a)). On the other hand, in the second straight pass (radially inward flow), the situation is reversed to the first straight pass: on the pressure and suction surfaces of the second straight pass, the buoyancy works in the opposing and aiding directions to the main flow, respectively(see Fig. 9(b)). In this way, when the buoyancy works, the radial flow direction becomes an important parameter which controls the flow and heat transfer in an orthogonally rotating channel. As seen in Figs. 4, 6 and 8 by being compared with Figs. 3, 5 and 7, when the centrifugal buoyancy is introduced, the effect of the aiding buoyancy contribution is seen in the larger variation of the streamwise shear stress on the pressure surface of the first straight pass, and in the reduced area of the reverse flow between the ribs on the suction surface of the second straight pass. These changes in the flow field cause the heat transfer on the corresponding surfaces larger, which may not be clear in Figs. 4 and 6, and it will be confirmed in the area-averaged Nusselt number later. The effect of the opposing buoyancy contribution is seen in the intensified and extended reverse flow region on the suction surface of the first straight pass, but the Nusselt number there shows a slight increase in the downstream part. This heat transfer increase due to the reverse flow seems contradicting, but the reason for this result will be explained by using the velocity and temperature fields later.

In order to examine the buoyancy effect in the most developed region in the present straight passes, the area-averaged Nusselt number at the downstream part of the straight pass is shown in Fig. 10. The averaging area between 5th and 6th ribs from the straight pass entrance (between 2nd and 3rd ribs from the downstream turn) was chosen so as for the flow and temperature fields to be most developed and at the same time to be still without the downstream turn effect. In Fig. 10, the buoyancy parameter, $Gr_{m,q}/Re_m^2$, is used as the horizontal axis. On the pressure surface, the buoyancy effect on Nu_{area} is larger than that on the suction surface, and Nu_{area} of the aiding contribution cases (solid lines) are larger than those of the opposing contribution cases (broken lines). This tendency is supported by the experimental results of the rib-roughened channel [14], although the entrance condition for the first straight pass in [14] was not disturbed by the upstream sharp

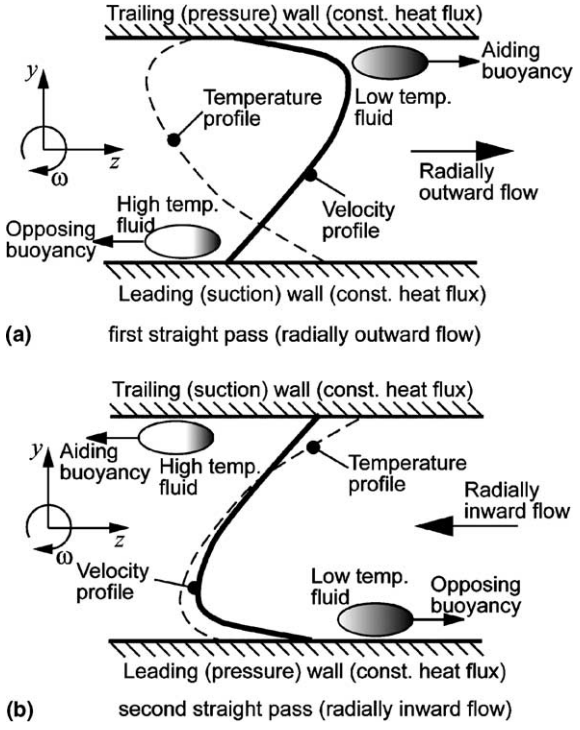

Fig. 9. Explanation of aiding and opposing buoyancy contributions in (a) first (radially outward flow) and (b) second (radially inward flow) straight passes.

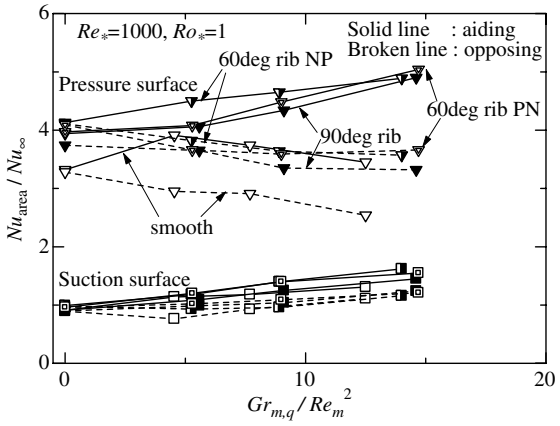

Fig. 10. Buoyancy effect on area-averaged Nusselt number at developed region in straight passes. (Averaging area was between 5th and 6th ribs from straight pass entrance. Open, filled, half-filled, and concentric symbols are for smooth, 90° rib, 60° rib NP, and 60° rib PN, respectively. Symbols with solid and broken lines are for aiding and opposing buoyancy contributions, respectively.)

turn. All the rib-roughened cases show the increase for the aiding contribution on the pressure surface as $Gr_{m,q}/Re_m^2$ increases. However, as seen in the figure, the smooth case once increases and then decreases as $Gr_{m,q}/Re_m^2$ increases. In [28], the smooth two-pass channel results showed that the buoyancy effect on the behavior of Nu_{area} at the developed region differed depending on Re_* and Ro_*, and therefore there is a possibility that the present monotonic behavior of Nu_{area} for the rib-roughened cases changes for different Re_* and Ro_* values. Nu_{area} on the suction surface show much smaller variation, and a slight increase is observed due to the buoyancy.

Figs. 11 and 12 show the contours of the time-averaged plane-normal velocity component ($\bar{u}$ or $\bar{w}$) and temperature, $\bar{\theta}$, respectively, for the 60° rib NP arrangement. Figs. (a) and (b) are for $Ra_* = 0$ and 2×10^4, respectively. In the figures, the values at nine different duct-axial locations are shown (see Fig. 2): from top to bottom $x = 4$, $z = 16.9$, 15, 13, 9, 5, 3, 1.1, and $x = 8$ (note that $z = 17$, 9, and 1 correspond to the tip of the inner wall of the turn A, the middle of the straight pass, and the tip of the inner wall of the turn B, respectively, and x and z are normalized by using $\ell = 0.5D$). The following descriptions on Figs. 11 and 12 are similar among the three rib arrangements.

Without the buoyancy (Figs. (a)), in the downstream region of the straight passes, the Coriolis force forms the uniform streamwise velocity profiles in the x direction on the suction side and the high temperature fluid covers the area. This uniform profile is caused by the Taylor–Proudman effect [41] due to the balance between the pressure gradient and the Coriolis force that does not have a component in the x direction. In the y–z mid-plane of the turn (top figure of Fig. 11(a)), the high momentum flow on the trailing side induces a dominating vortex that rotates in the counter-clockwise direction in the figure. Due to this strong vortex, the high momentum and low temperature fluid on the trailing side is transported to the leading side. At this y–z mid-plane, the reverse flow region is seen at the central region. After the turn, the strong vortex dominates at the turn outlet ($z = 16.9$) and at $z = 15$, but then the Coriolis force modifies the flow field uniform in the x direction again at the downstream locations.

When the buoyancy is introduced (Figs. (b)), the opposing buoyancy contribution is observed in the extended reverse flow region that is clearly seen on the rib-windward side near the suction surface in the first straight pass ($1 < x < 3$) for $z = 9$–15 (that can also be confirmed by the negative shear stress region in Fig. 6(b)). When Fig. 12(a) and (b) are compared to each other, the temperature profiles corresponding to the buoyancy-induced reverse flow region near the suction surface of the first straight pass (see $1 < x < 3$ for $z = 9$–15 in Fig. 12(b)) give the smaller temperature gradient there, and the temperature there becomes lower as compared to that of $Ra_* = 0$ (Fig. 12(a)). This is the reason for the heat transfer increase due to the opposing buoyancy contribution on the suction surface of the first straight pass observed in Figs. 4, 6 and 8. The reason for the formation of this low temperature region can be understood by the increased turbulent transport induced by the increased shear rate in the mixing layer between the reverse flow and the main flow, and this will be confirmed later by the increased turbulent kinetic energy at the corresponding region. Near the suction surface of the second straight pass in Fig. 11(b), the aiding contribution of the centrifugal buoyancy accelerates the flow, and the rib-induced flow separation area becomes clearer on the rib-leeward side in Fig. 11(b) ($5 < x < 7$ for $z = 3$–9). This contributes to convect the low temperature fluid to the suction surface in the second straight pass as can be seen by comparing Fig. 12(a) and (b) (see $5 < x < 7$ for $z = 3$–9).

Fig. 13 shows the turbulent kinetic energy, k, calculated from the grid resolvable components at the same locations as Figs. 11 and 12. In Fig. 13, out-of-range high values are shown by solid black area, and note that the range is different in and around the sharp turn because of the high values there. The heat transfer enhancement caused by the centrifugal buoyancy on the pressure surface in the first straight pass (radially outward flow) was explained by the turbulence production due to the increased shear stress by the buoyancy [11], and, as seen in Fig. 13, k is increased in the vicinity of the trailing (pressure) wall in the first straight pass. As mentioned above, k near the suction surface of the first straight pass is increased by the increased shear rate in the mixing layer between the reverse flow and the main flow. This high k region locates at a certain distance from the suction surface as seen in Fig. 13(b) ($1 < x < 3$ for $z = 9$–15), and it contributes to the turbulent mixing between the low temperature fluid of the main flow and the high temperature fluid in the reverse flow region. When the radially outward and inward flows are compared, k is more intensified in the radially outward flow (the first straight pass) than that in the radially inward flow (the second straight pass). These characters are similar among the three rib arrangements (figures not shown).

In order to view the flow structure of the whole two-pass channel, the isosurface (surface with the same value) of the second invariant, Q, of the deformation tensor, $\partial u_i/\partial x_j$, [42] is shown in Fig. 14. The value of Q is calculated by Eq. (16) for incompressible fluids, and it is often used to identify vortices because the positive value of Q means that the vorticity exceeds the strain.

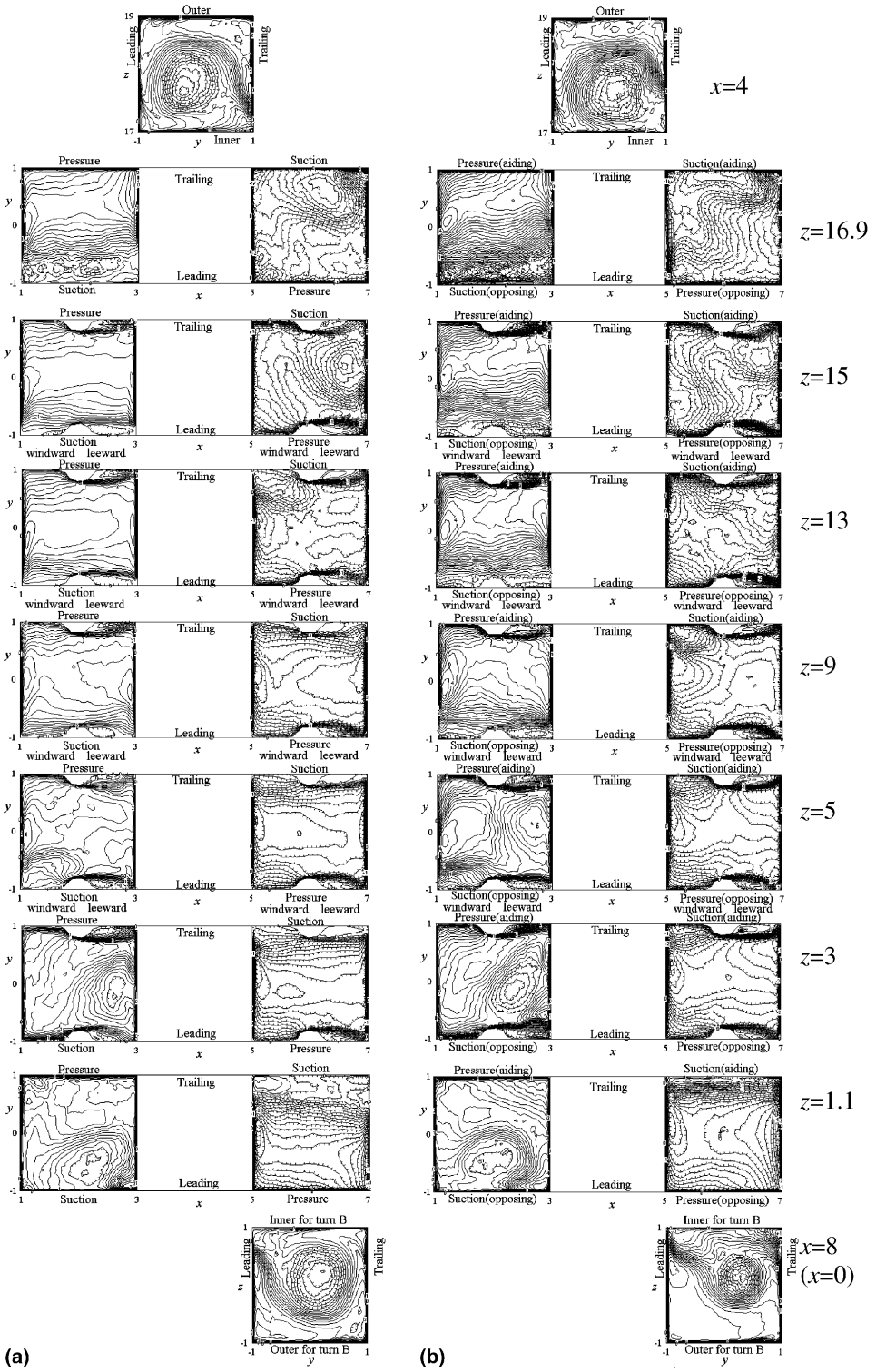

Fig. 11. Buoyancy effect on time-averaged plane-normal velocity component in planes normal to duct-axis for 60° rib NP of $Re_* = 1000$ and $Ro_* = 1$. (From top to bottom, $x = 4$, $z = 16.9$, 15, 13, 9, 5, 3, 1.1, and $x = 8$. Contour lines are drawn by every 0.2.) (a) $Ra_* = 0$ and (b) $Ra_* = 2 \times 10^4$.

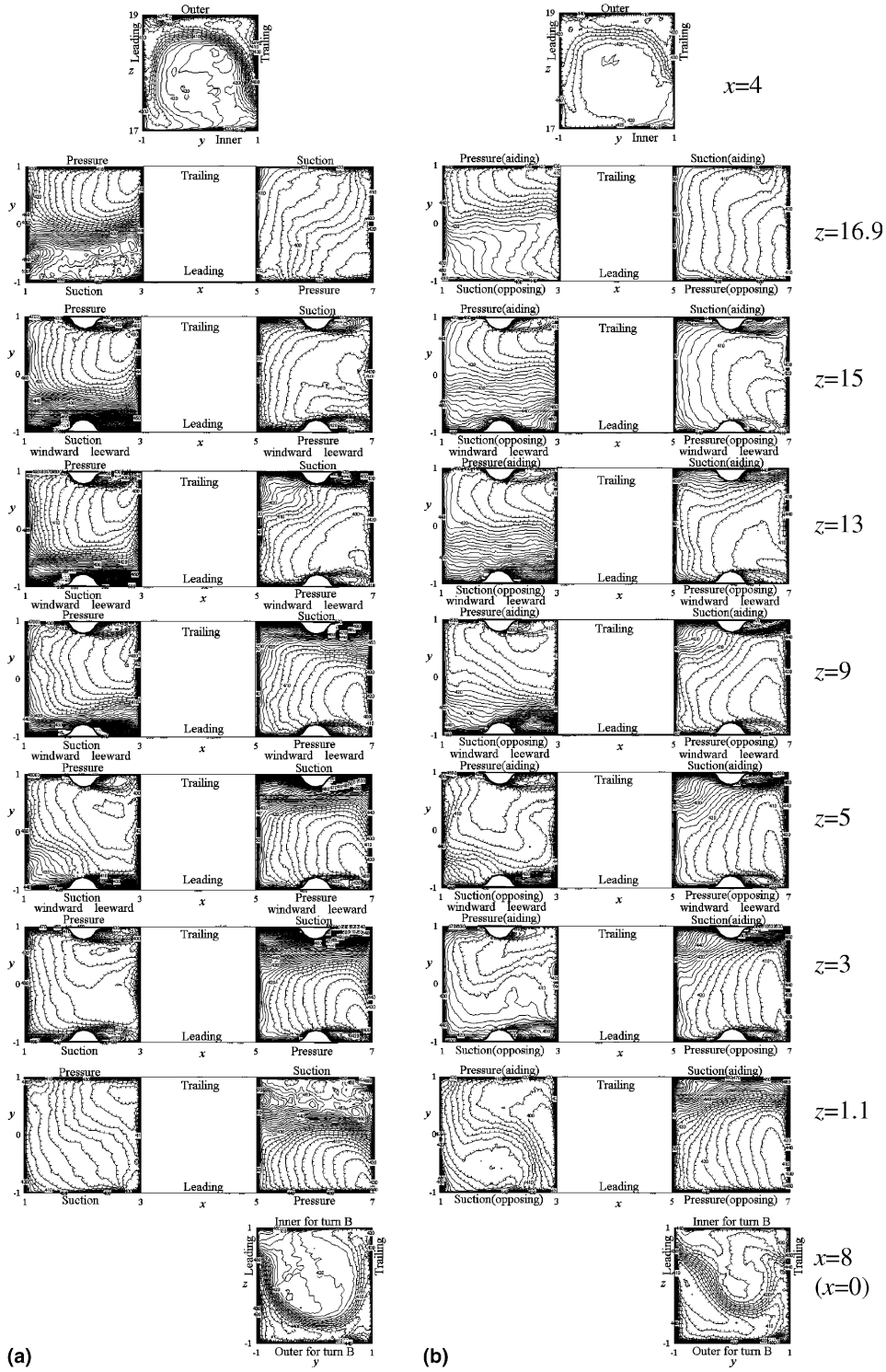

Fig. 12. Buoyancy effect on time-averaged temperature in planes normal to duct-axis for 60° rib NP of $Re_* = 1000$ and $Ro_* = 1$. (From top to bottom, $x = 4$, $z = 16.9$, 15, 13, 9, 5, 3, 1.1, and $x = 8$. Contour lines are drawn by every 2.) (a) $Ra_* = 0$ and (b) $Ra_* = 2 \times 10^4$.

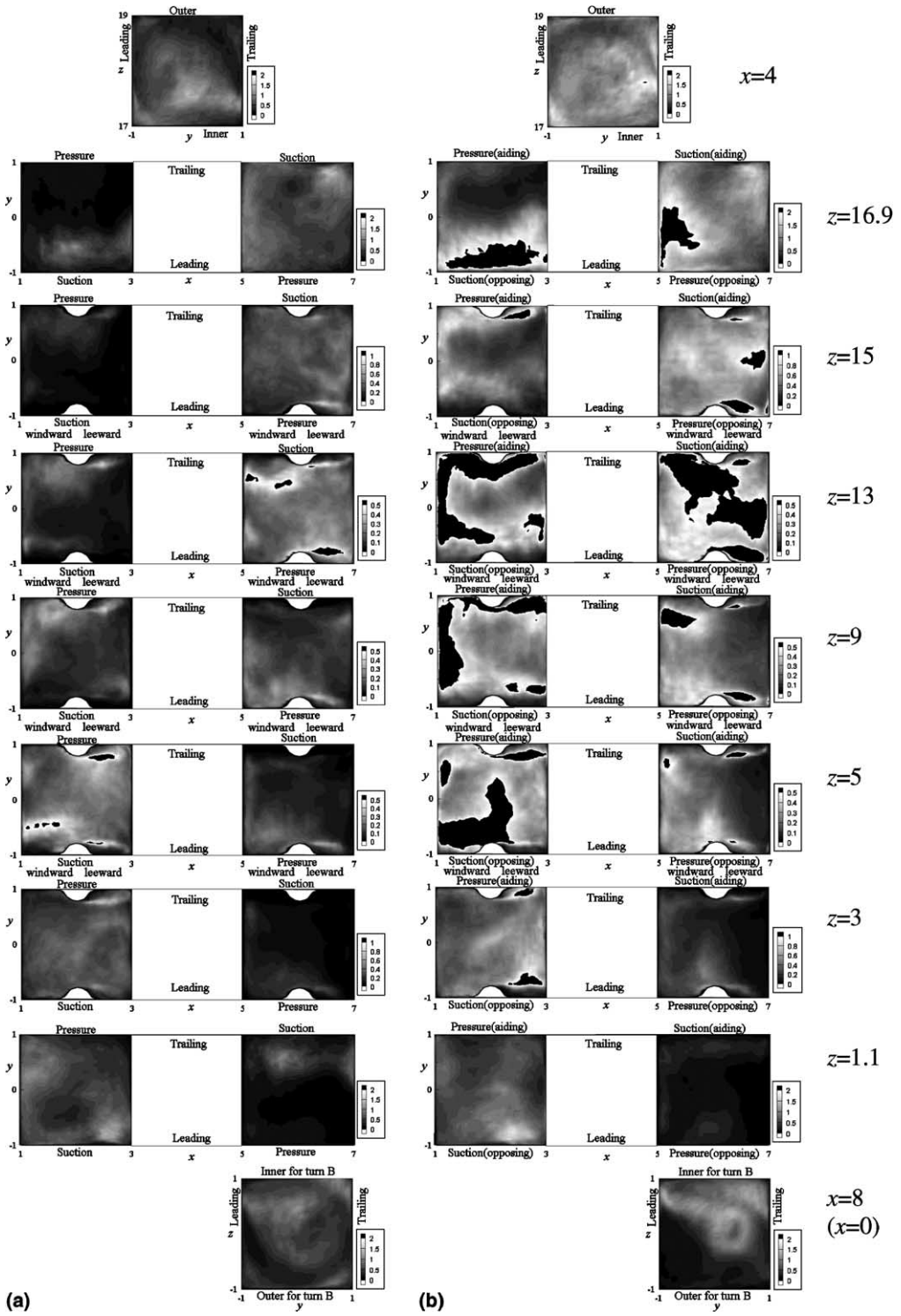

Fig. 13. Buoyancy effect on turbulent kinetic energy in planes normal to duct-axis for 60° rib NP of $Re_* = 1000$ and $Ro_* = 1$. (From top to bottom, $x = 4$, $z = 16.9$, 15, 13, 9, 5, 3, 1.1, and $x = 8$.) (a) $Ra_* = 0$ and (b) $Ra_* = 2 \times 10^4$.

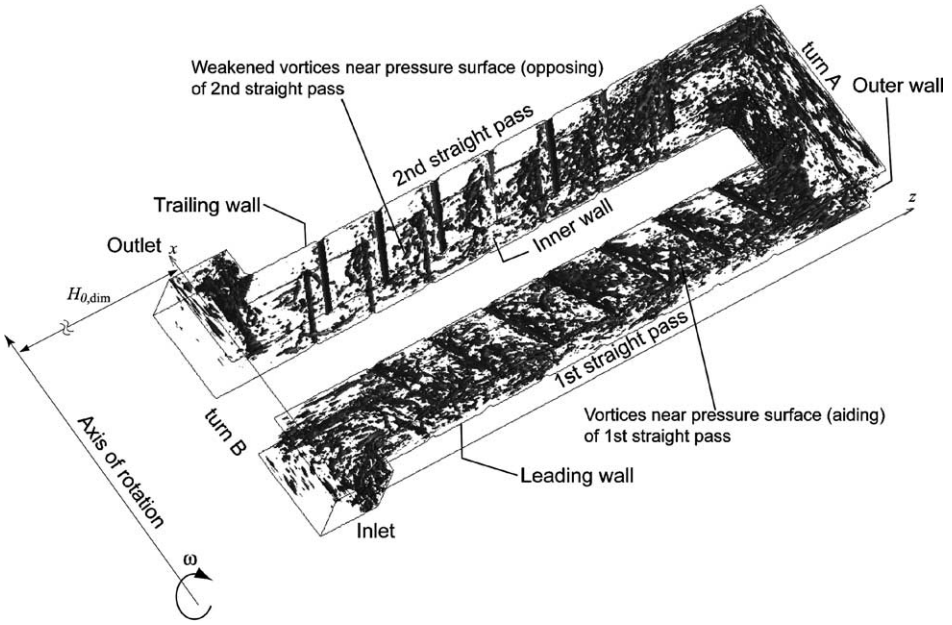

Fig. 14. Instantaneous vortex structure visualized as isosurface of $Q = 100$ (60° rib NP, $Re_* = 1000$, $Ro_* = 1$, and $Ra_* = 2 \times 10^4$).

$$Q = \frac{1}{2}\left[\left(\frac{\partial u_i}{\partial x_i}\right)^2 - \left(\frac{\partial u_i}{\partial x_j}\right)\left(\frac{\partial u_j}{\partial x_i}\right)\right] = -\frac{1}{2}\left(\frac{\partial u_i}{\partial x_j}\right)\left(\frac{\partial u_j}{\partial x_i}\right) = \frac{1}{2}\left\{\left[\frac{1}{2}\left(\frac{\partial u_i}{\partial x_j} - \frac{\partial u_j}{\partial x_i}\right)\right]^2 - \left[\frac{1}{2}\left(\frac{\partial u_i}{\partial x_j} + \frac{\partial u_j}{\partial x_i}\right)\right]^2\right\}. \quad (16)$$

As seen in Fig. 14, in and around the turn the strong vortices are produced. The effect of the buoyancy is seen in the different number density of the vortex near the pressure surfaces in the first and second straight passes: in the first straight pass, the number of the strong vortex is larger due to the aiding contribution of the buoyancy. In the second straight pass, the vortex is weakened due to the opposing contribution of the buoyancy, and the number of the strong vortex becomes smaller. As compared with the smooth channel results of [28], the angled rib installation energizes the vortices in the straight pass, and at the same time it makes the streamwise size of the vortex shorter and the axis of the vortex inclined with respect to the channel axis in the straight pass. The longitudinal vortex which had a long streamwise length observed in the smooth channel [28] cannot be seen in the rib-roughened case due to the disturbances induced by the periodic ribs.

In [27], the rib orientation effect was clearly observed in the stationary condition between the 60° rib NP and PN cases: in the NP arrangement, the upstream-rib-induced and sharp-turn-induced secondary flow directions were opposite which resulted in the enhanced heat transfer in the turn, and after the turn the coincidence between the sharp-turn-induced and downstream-rib-induced secondary flow directions maintained the high heat transfer. On the other hand, in the PN arrangement, the situation was reversed, and the heat transfer in and after the turn was less enhanced. In Fig. 15(b), the time-averaged secondary velocity vector, $(\bar{u}, \bar{v})$, plane-normal velocity, $\bar{w}$, and temperature, $\bar{\theta}$, for the 60° rib PN case are shown at two duct-axial locations ($z = 13$ and 5) which can be compared with the counterparts in Figs. 15(a), 11 and 12. Without the buoyancy, the phenomena just after the turn is dominated by the turn-induced flow, and therefore the profiles after the turn become similar between the 60° rib NP and PN cases for a certain distance from the turn (figures not shown for the PN case). When the fluid flows to the downstream region of the straight pass, the difference between the NP and PN cases is caused only by the rib orientation, and therefore the profiles of $\bar{w}$ for NP and PN cases must approach to the mirror symmetry to each other with respect to the bisector parallel to the y axis which is confirmed in Figs. 11(a) and 15(left). However, the profiles of $\bar{\theta}$ for the NP and PN cases stay similar to each other and do not show the above-mentioned mirror symmetry to each other as seen in Figs. 12(a) and 15(left). When the centrifugal buoyancy works, the aiding and opposing contributions of the centrifugal buoyancy modify the flow, and because of the different rib orientation between the NP and PN cases, the

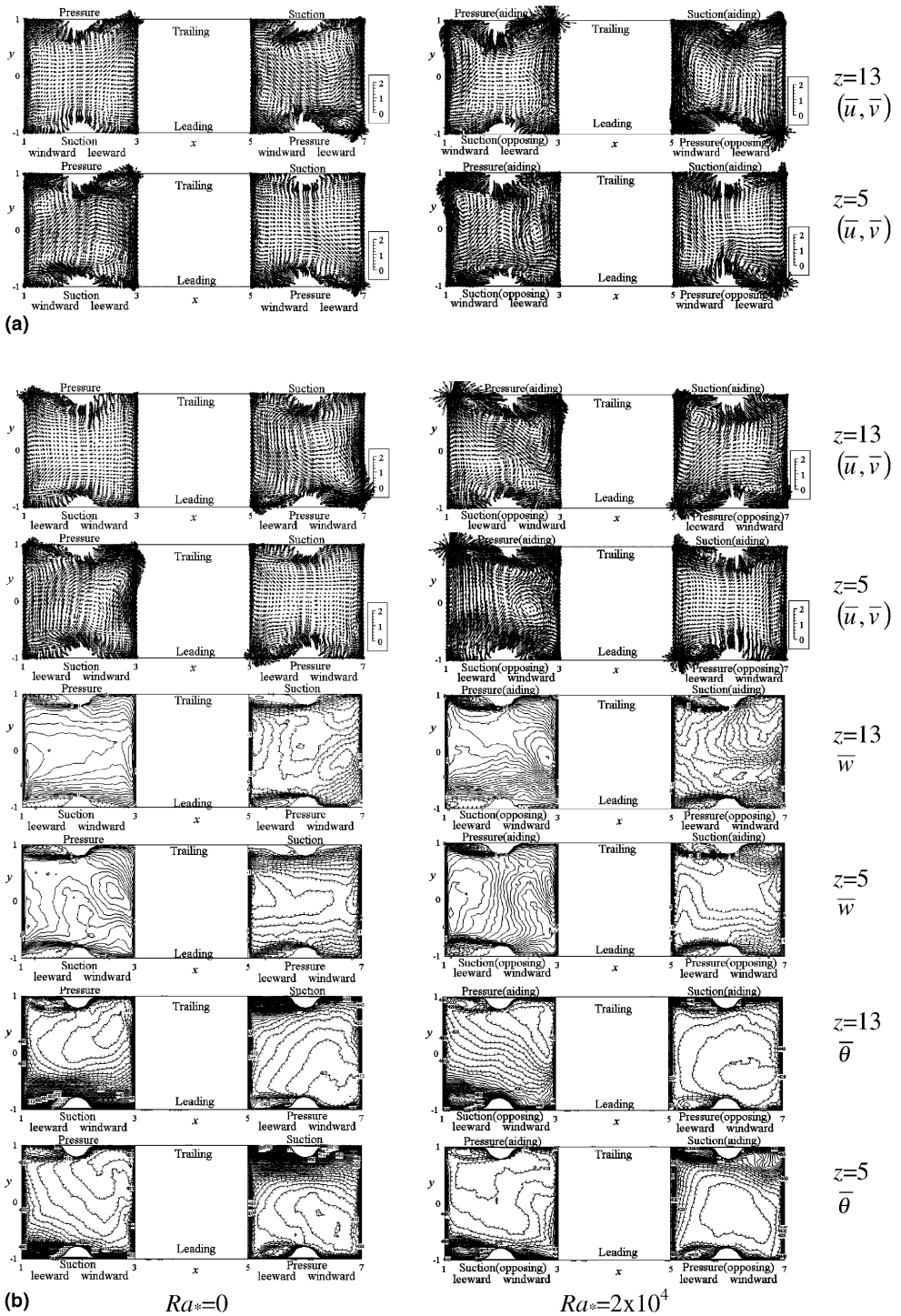

Fig. 15. Buoyancy and rib orientation effects on time-averaged fields in planes normal to duct-axis: (a) 60° rib NP; (b) 60° rip PN.

profiles of $\bar{w}$ and $\bar{\theta}$ become different from those of $Ra_* = 0$: especially the difference in $\bar{\theta}$ is large as seen by comparing Fig. 15(b) (bottom-right two figures) with Fig. 12(b). In the second straight pass, the suction surface comes to the aiding contribution side, and the fluid is accelerated there, which intensifies the velocity com-

ponent along the angled rib (the rib-induced secondary flow). As a result, the flow field is modified toward the similar situation to the stationary condition where the two rib-roughened surfaces equally contribute to the rib-induced secondary flow, and the low temperature peak in the second straight pass (bottom-right figure in Fig. 15(b)) shifts to the inner wall side as compared to that of the 60° rib NP case ($z = 5$ in Fig. 12(b)).

Fig. 16 shows the friction factor, f, normalized by using f_B in the following Blasius equation:

$$f_B = 0.079 Re_m^{-0.25}. \tag{17}$$

The precise values of f/f_B are shown in Table 1. In order to decompose the total pressure loss into the sharp-turn and straight-pass contributions, the following pressure loss coefficients, K_{turn} and $K_{straight}$, are also plotted in Fig. 16 [43]:

$$K_{turn} = \frac{\Delta p_{turn}}{\frac{1}{2}\rho U_m^2} \quad \text{and} \quad K_{straight} = \frac{\Delta p_{straight}}{\frac{1}{2}\rho U_m^2}. \tag{18}$$

Here, Δp_{turn} is the pressure loss associated with the sharp turn, and it is calculated by linearly extrapolating the area-averaged wall-pressure profile at the central region of the first and second straight passes in the direction toward the turn inlet and outlet locations at $z = 17$ for the turn A and at $z = 1$ for the turn B [43]. The area-average was taken with the streamwise pitch of D in the straight pass. The straight pass component, $\Delta p_{straight}$, was calculated from the linear pressure profile at the central region of the straight pass. A decrease of the f factor by the buoyancy force is observed in Fig. 16. Without the buoyancy, K_{turn} is larger than $K_{straight}$. The buoyancy makes K_{turn} decrease both in the turns A and B, although the decrease in the turn A is less. The value of $K_{straight}$ in the second straight pass becomes negative, due to the positive pressure gradient in the streamwise direction which is caused by the coincidence of the main flow and buoyancy force directions: the main flow is driven by the buoyancy in the second straight pass (radially inward flow). This situation resulted in the suppressed k in Fig. 13(b) and the weakened vortices in Fig. 14 in the second straight pass as compared to the first straight pass. The buoyancy increases and decreases $K_{straight}$ in the first and second straight passes, respectively, and this opposing variation in $K_{straight}$ cancels to each other. As a total, the pressure loss behavior of the channel is controlled by K_{turn} and the f factor decreases as $Gr_{m,q}/Re_m^2$ increases. As can be seen in the figure, these tendencies are the same as the smooth channel case (open symbols in the figure).

Fig. 17 shows Colburn's j factor normalized by using j_∞ calculated from Nu_∞ in Eq. (15). The precise values of j/j_∞ are shown in Table 1. In order to further examine the heat transfer efficiency taking the pressure loss into account, the heat transfer efficiency index, η_{eff}, was calculated by using the following equation [44]:

$$\eta_{eff} = \frac{St/St_{smooth,stationary}}{(f/f_{smooth,stationary})^{1/3}}. \tag{19}$$

As explained in [44], η_{eff} is the index of the heat conductance for equal pumping power and heat transfer surface area. As shown in Fig. 17, the j factor is insensitive to the buoyancy and stays almost constant. As a result, η_{eff} slightly increases with the increase of the buoyancy due to the decreased f factor seen in Fig. 16. Among the three rib arrangements, η_{eff} becomes almost same within the present buoyancy parameter range, and it is slightly higher than the smooth channel case.

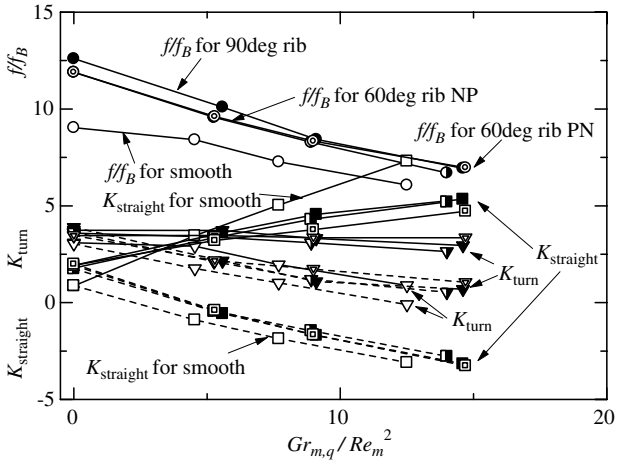

Fig. 16. Buoyancy effect on pressure loss for $Re_* = 1000$ and $Ro_* = 1$. (Legend for the symbols are the same as that in Fig. 10. Symbols for K_{turn} and $K_{straight}$ with solid lines are for turn A or first straight pass, and those with broken lines are for turn B or second straight pass.)

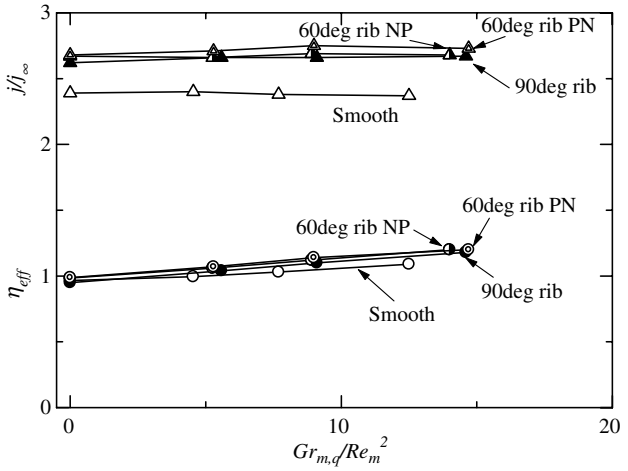

Fig. 17. Buoyancy effect on j factor and heat transfer efficiency index (legend for the symbols are the same as that in Fig. 10).

4. Conclusions

The large eddy simulation of the two-pass rib-roughened square channel with the 180° sharp turns was performed changing the Rayleigh number for three different rib arrangements (the 90° rib, the 60° rib NP, and the 60° rib PN cases). From the numerical results the following conclusions were drawn.

When the centrifugal buoyancy was introduced, the aiding and opposing contributions of the centrifugal buoyancy worked in the different way depending on the radial flow directions (radially outward and inward flows). The pressure surfaces of the radially outward and inward flows came to the aiding and opposing buoyancy contribution sides, and there the heat transfer was enhanced and suppressed, respectively. On the other hand, the suction surfaces of the radially outward and inward flows came to the opposing and aiding buoyancy contribution sides, respectively, and both showed the slightly increased heat transfer. The heat transfer enhancement due to the opposing buoyancy contribution on the suction surface was caused by the intensified turbulent transport as a result of the increased shear rate at the mixing layer between the reverse flow and the main flow.

The friction factor was decreased as the buoyancy increased which was dominated by the sharp-turn induced pressure loss because the increased and decreased pressure losses in the first and second straight passes, respectively, cancelled to each other. On the other hand, the channel averaged Nusselt number was insensitive to the buoyancy, and it was almost constant. The heat transfer efficiency index taking the pressure loss into account gave the almost same values for the three rib arrangements of this study within the present buoyancy parameter range.

References

[1] J.-C. Han, Recent studies in turbine blade cooling, in: CD-ROM Proceedings of the 9th International Symposium on Transport Phenomena and Dynamics of Rotating Machinery, Honolulu, Hawaii, US, Invited Lecture, 2002, pp. 1–16.

[2] A. Murata, S. Mochizuki, M. Fukunaga, Detailed measurement of local heat transfer in a square-cross-section duct with a sharp 180-deg turn, in: Heat Transfer 1994, Proceedings of the International Heat Transfer Conference, Brighton, GB, vol. 4, 1994, pp. 291–296.

[3] S. Mochizuki, A. Murata, M. Fukunaga, Effects of rib arrangements on pressure drop and heat transfer in a rib-roughened channel with a sharp 180° turn, Trans. ASME J. Turbomach. 119 (1997) 610–616.

[4] P.R. Chandra, J.C. Han, S.C. Lau, Effect of rib angle on local heat/mass transfer distribution in a two-pass rib-roughened channel, Trans. ASME J. Turbomach. 110 (1988) 233–241.

[5] M. Hirota, H. Fujita, A. Syuhada, S. Araki, T. Yoshida, T. Tanaka, Heat/mass transfer characteristics in two-pass smooth channels with a sharp 180-deg turn, Int. J. Heat Mass Transfer 42 (1999) 3757–3770.

[6] S.V. Ekkad, J.C. Han, Detailed heat transfer distributions in two-pass square channels with rib turbulators, Int. J. Heat Mass Transfer 40 (11) (1997) 2525–2537.

[7] T.M. Liou, C.C. Chen, T.W. Tsai, Liquid crystal measurements of heat transfer in a 180° sharp turning duct with different divider thicknesses, CD-ROM Proceedings of the 8th International Symposium on Flow Visualization, Sorrento, Italy, vol. 71, 1998, pp. 1–9.

[8] T. Astarita, G. Cardone, Thermofluidynamic analysis of the flow in a sharp 180° turn channel, Exp. Thermal Fluid Sci. 20 (2000) 188–200.

[9] S.Y. Son, K.D. Kihm, J.-C. Han, PIV flow measurements for heat transfer characterization in two-pass square channels with smooth and 90° ribbed walls, Int. J. Heat Mass Transfer 45 (2002) 4809–4822.

[10] J.-C. Han, Y.-M. Zhang, K. Kalkuehler, Uneven wall temperature effect on local heat transfer in a rotating two-pass square channel with smooth walls, Trans. ASME J. Heat Transfer 115 (1993) 912–920.
[11] J.H. Wagner, B.V. Johnson, F.C. Kopper, Heat transfer in rotating serpentine passages with smooth walls, Trans. ASME J. Turbomach. 113 (1991) 321–330.
[12] S. Mochizuki, J. Takamura, S. Yamawaki, W.-J. Yang, Heat transfer in serpentine flow passages with rotation, Trans. ASME J. Turbomach. 116 (1994) 133–140.
[13] J.A. Parsons, J.-C. Han, Y.-M. Zhang, Effect of model orientation and wall heating condition on local heat transfer in a rotating two-pass square channel with rib turbulators, Int. J. Heat Mass Transfer 38 (7) (1995) 1151–1159.
[14] B.V. Johnson, J.H. Wagner, G.D. Steuber, F.C. Yeh, Heat transfer in rotating serpentine passages with trips skewed to the flow, Trans. ASME J. Turbomach. 116 (1994) 113–123.
[15] S. Mochizuki, M. Beier, A. Murata, T. Okamura, Y. Hashidate, Detailed measurement of convective heat transfer in rotating two-pass rib-roughened coolant channels, ASME Paper, 96-TA-6, 1996.
[16] T.-M. Liou, C.-C. Chen, M.-Y. Chen, TLCT and LDV measurements of heat transfer and fluid flow in a rotating sharp turning duct, Int. J. Heat Mass Transfer 44 (2001) 1777–1787.
[17] B. Banhoff, U. Tomm, B.V. Johnson, I. Jennions, Heat transfer predictions for rotating U-shaped coolant channels with skewed ribs and with smooth walls, ASME Paper, 97-GT-162, 1997.
[18] Y.-L. Lin, T.I.-P. Shih, M.A. Stephens, M.K. Chyu, A numerical study of flow and heat transfer in a smooth and ribbed U-duct with and without rotation, Trans. ASME J. Heat Transfer 123 (2001) 219–232.
[19] A. Huser, S. Biringen, Direct numerical simulation of turbulent flow in a square duct, J. Fluid Mech. 257 (1993) 65–95.
[20] S. Gavrilakis, Numerical simulation of low Reynolds number turbulent flow through a straight square duct, J. Fluid Mech. 244 (1992) 101–129.
[21] R.K. Madabhushi, S.P. Vanka, Large eddy simulation of turbulence-driven secondary flow in a square duct, Phys. Fluids A 3 (11) (1991) 2734–2745.
[22] A. Murata, S. Mochizuki, Effect of cross-sectional aspect ratio on turbulent heat transfer in an orthogonally rotating rectangular smooth duct, Int. J. Heat Mass Transfer 42 (1999) 3803–3814.
[23] J. Pallares, L. Davidson, Large eddy simulations of turbulent flow in a rotating square duct, Phys. Fluids 12 (11) (2000) 2878–2894.
[24] A. Murata, S. Mochizuki, Large eddy simulation of turbulent heat transfer in an orthogonally rotating square duct with angled rib turbulators, Trans. ASME J. Heat Transfer 123 (2001) 858–867.
[25] A. Murata, S. Mochizuki, Effect of centrifugal buoyancy on turbulent heat transfer in an orthogonally rotating square duct with transverse or angled rib turbulators, Int. J. Heat Mass Transfer 44 (2001) 2739–2750.
[26] A. Murata, S. Mochizuki, Large eddy simulation of turbulent heat transfer in a rotating two-pass smooth square channel with sharp180-deg turns, Int. J. Heat Mass Transfer 47 (2004) 683–698.
[27] A. Murata, S. Mochizuki, Effect of rib orientation and channel rotation on turbulent heat transfer in a two-pass square channel with sharp 180-deg turns investigated by using large eddy simulation, Int. J. Heat Mass Transfer 47 (2004) 2599–2618.
[28] A. Murata, S. Mochizuki, Centrifugal buoyancy effect on turbulent heat transfer in a rotating two-pass smooth square channel with sharp 180-deg turns, Int. J. Heat Mass Transfer, in press (No. KS/SN 03-029s).
[29] M.E. Taslim, S.D. Spring, Effect of turbulator profile and spacing on heat transfer and friction in a channel, J. Thermophys. Heat Transfer 8 (3) (1994) 555–562.
[30] G.J. Korotky, M.E. Taslim, Rib heat transfer coefficient measurements in a rib-roughened square passage, ASME Paper, 96-GT-356, 1996.
[31] M.E. Taslim, T. Li, D.M. Kercher, Experimental heat transfer and friction in channels roughened with angled, V-shaped, and discrete ribs on two opposite walls, Trans. ASME J. Turbomach. 118 (1996) 20–28.
[32] J.C. Han, J.S. Park, C.K. Lei, Heat transfer enhancement in channels with turbulence promoters, Trans. ASME. J. Eng. Gas Turbines Power 107 (1985) 628–635.
[33] S.V. Patankar, C.H. Liu, E.M. Sparrow, Fully developed flow and heat transfer in ducts having streamwise-periodic variations of cross-sectional area, Trans. ASME J. Heat Transfer 99 (1977) 180–186.
[34] T. Kajishima, T. Ohta, K. Okazaki, Y. Miyake, High-order finite-difference method for incompressible flows using collocated grid system, JSME Int. J. B 41 (4) (1998) 830–839.
[35] C. Meneveau, T.S. Lund, W.H. Cabot, A Lagrangian dynamic subgrid-scale model of turbulence, J. Fluid Mech. 319 (1996) 353–385.
[36] P. Moin, K. Squires, W. Cabot, S. Lee, A dynamic subgrid-scale model for compressible turbulence and scalar transport, Phys. Fluids A 3 (11) (1991) 2746–2757.
[37] F.H. Harlow, J.E. Welch, Numerical calculation of time-dependent viscous incompressible flow of fluid with free surface, Phys. Fluids 8 (12) (1965) 2182–2189.
[38] J. Kim, P. Moin, Application of a fractional-step method to incompressible Navier–Stokes equations, J. Comput. Phys. 59 (1985) 308–323.
[39] Y. Zang, R.L. Street, J.R. Koseff, A non-staggered grid, fractional step method for time-dependent incompressible Navier–Stokes equations in curvilinear coordinates, J. Comput. Phys. 114 (1994) 18–33.
[40] W.M. Kays, M.E. Crawford, Convective Heat and Mass Transfer, third ed., McGraw-Hill, New York, 1993, p. 316.
[41] G.K. Batchelor, An Introduction to Fluid Dynamics, Cambridge University Press, 1967, pp. 555–559.
[42] J.C.R. Hunt, A.A. Wray, P. Moin, Eddies, stream, and convergence zones in turbulent flows, Center for Turbulence Research Report, CTR-S88, 1988.
[43] D.E. Metzger, C.W. Plevich, C.S. Fan, Pressure loss through sharp180° turns in smooth rectangular channels, J. Eng. Gas Turbines Power 106 (1984) 677–681.
[44] D.L. Gee, R.L. Webb, Forced convection heat transfer in helically rib-roughened tubes, Int. J. Heat Mass Transfer 23 (1980) 1127–1136.